

# Spatial analysis of polarimetric images to enhance near-surface sampling sensitivity: feasibility in demineralized teeth and other tissue-like media

Michael D. Singh<sup>a,\*</sup>, Lothar Lilge<sup>a,b</sup> and Alex Vitkin<sup>a,b,c</sup>

<sup>a</sup>University of Toronto, Department of Medical Biophysics, Temerty Faculty of Medicine, Toronto, Ontario, Canada

<sup>b</sup>University Health Network, Princess Margaret Cancer Centre, Toronto, Ontario, Canada

<sup>c</sup>University of Toronto, Temerty Faculty of Medicine, Department of Radiation Oncology, Toronto, Ontario, Canada

---

**ABSTRACT.** **Significance:** Early tooth demineralization may be detectable through spatial analysis of polarized light images as demonstrated in this study. This may also prove useful in the early detection of epithelial tumors that comprise the majority of the cancer burden worldwide.

**Aim:** The spatial properties of polarized light images have not been greatly exploited in biomedicine to improve sensitivity to superficial tissue regions; therefore, we investigate the optical sampling depth effects as a function of location in the back-scattered polarimetric images.

**Approach:** Backscattered linear polarization intensity distributions exhibit four-lobed patterns arising through single-scattering, multiple-scattering, and geometrical effects. These photon pathway dynamics are investigated through experimental imaging of microsphere suspensions along with corroborative computational polarization-sensitive Monte Carlo modeling. The studied sampling depth effects of linear and circular polarization images (explored in a previous study) are then evaluated on normal and demineralized human teeth, which are known to differ in their surface and sub-surface structures.

**Results:** Backscattered linear polarization images exhibit enhanced sensitivity to near-surface properties of media (for example, surface roughness and turbidity) at specific locations within the four-lobed patterns. This yields improved differentiation of two tooth types when spatially selecting image regions in the direction perpendicular to the incident linear polarization vector. Circular polarimetric imaging also yields improved differentiation through spatial selection of regions close to the site of illumination. Improved sensitivity to superficial tissues is achieved through a combination of these linear and circular polarimetric imaging approaches.

**Conclusions:** Heightened sampling sensitivity to tissue microstructure in the surface/near-surface region of turbid tissue-like media and dental tissue is achieved through a judicious spatial selection of specific regions in the resultant co-linear and cross-circular backscattered polarimetric images.

© The Authors. Published by SPIE under a Creative Commons Attribution 4.0 International License. Distribution or reproduction of this work in whole or in part requires full attribution of the original publication, including its DOI. [DOI: [10.1117/1.JBO.28.10.102906](https://doi.org/10.1117/1.JBO.28.10.102906)]

**Keywords:** polarimetry; linear and circular polarization; penetration/sampling depth; biomedical optics; dental caries; Monte Carlo

Paper 230158SSR received May 29, 2023; revised Jul. 22, 2023; accepted Jul. 31, 2023; published Sep. 9, 2023.

---

\*Address all correspondence to Michael D. Singh, [michaeldhillon.singh@mail.utoronto.ca](mailto:michaeldhillon.singh@mail.utoronto.ca)

## 1 Introduction

Polarization gating has been used in biophotonics to probe superficial tissue regions by filtering away deeply penetrating depolarized light.<sup>1</sup> Notable early demonstrations of this include the works of Anderson et al.<sup>2</sup> and Jacques et al.,<sup>3,4</sup> which employed linear co- and crossed-polarization configurations to enhance visualization of dermatologic features and pathologies. The Feld group<sup>5-7</sup> applied this type of filtering to optimize measurements of cell nuclear size in epithelial tissue for cancer detection applications. These “simple” polarization-filtering methods have been advanced in combination with other modalities, such as coherence-gating,<sup>8,9</sup> temporal-gating,<sup>10-12</sup> depolarization,<sup>13-17</sup> and illumination property considerations (e.g., intensity, angle, and wavelength),<sup>18-22</sup> to gain greater control over sampling depths and enable characterization of superficial tissues and pathologies. Yet it seems as if polarization-sensitive light collection properties (geometry, detector size, ROI selection, etc.)<sup>18</sup> have thus far not been greatly exploited to enhance depth selectivity.

Our previous study<sup>23</sup> showed that useful depth sensitivity can be achieved through judicious selection of specific regions within backscattered circular co- and crossed-polarization images (i.e., helicity-preserved and helicity-flipped images, respectively). Specifically, helicity-flipping typically occurs after reflection-like large-angle backward-scattering events, whereas helicity-preservation occurs after small-angle forward-scattering events [see Fig. 1(a)]. Due to these scattering-angle-dependent responses, helicity-flipped light offers shallower sampling since it can be redirected into the backward hemisphere through a single reflection-like event, whereas helicity-preserved photons must be forward-scattered in an arc-like trajectory, which generally results in deeper penetration [see Fig. 1(b)].<sup>24-26</sup> The superficial sensitivity of helicity-flipped light can then be further enhanced by spatially selecting the region that is closer to the illuminated spot since penetration depth generally increases with radial distance.

Notably, linearly polarized backscattered light can also exhibit co- and cross-spatial behavior with corresponding sensitivity to sampling depth,<sup>25,27</sup> although arguably in a more complex fashion. Namely, four-lobed patterns emerge in co- and cross-linear images, such as those observed in early polarized light images of the human eye,<sup>28-30</sup> atmospheric clouds,<sup>31,32</sup> and other media, which have generated much curiosity (originally termed “polarization cross” patterns). These patterns are a result of interplays between single- and multiple-scattering effects of linearly polarized light. The sampling depths along certain directions of these patterns evidently offer shallower sampling depths. Though these patterns have been investigated,<sup>33-36</sup> to the best of our

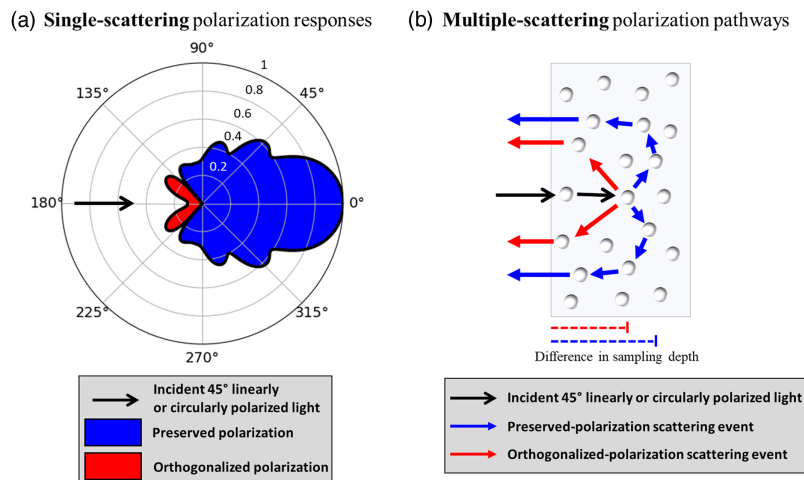


**Fig. 1** Polarization-dependent single-scattering and multiple-scattering effects. (a) Polar plot showing the scattered 45 deg linear and circular polarization intensities from incident 45 deg linearly and circularly polarized light, respectively, and color-coded red/blue to indicate orthogonalization/preservation. It is observed that light is orthogonalized in the backward-scatter direction (135 deg to 225 deg). (b) The single-scattering responses in (a) suggest that orthogonalized and polarization-state-preserving photons undergo characteristic multiple-scattering pathways in turbid media, such that the former penetrate less deeply. Figures adapted from Ref. 23.

knowledge they have not been exploited for their photon pathlengths/depth sensitivity characteristics.

To extend our previous work on circular polarization and depth sampling,<sup>23</sup> here we investigate backscattered linear polarization patterns to gain insight into their sampling depth distributions. This is achieved through experimental imaging of polystyrene microspheres along with theoretical analysis, including single-scattering mathematics and corroborative Monte Carlo simulation statistics (e.g., intensity and scattering count distributions). It is demonstrated that superficial sensitivity to media can be enhanced through specific region selection of co-linear polarimetric images. Coupled with our earlier investigation of backscattered circularly polarized light patterns,<sup>23</sup> a powerful composite polarimetry platform for differential depth sensitivity in an otherwise depth-unresolved technique emerges.

To assess the utility of this approach, we then applied it to differentiate normal and decayed human teeth, which exhibit different surface/sub-surface structural and compositional properties. It is found that optimal differentiation is achieved through specific spatial selection of polarimetric image regions using both linearly and circularly polarized light. The encouraging results may prove useful for the detection of early tooth decay, an important pre-requisite for effective intervention.<sup>37,38</sup> Early tooth decay detection remains challenging due to the shallowness of demineralization in its early stages,<sup>39</sup> highlighting the potential of our polarimetric method; however, future studies on larger sample sizes are needed. Nonetheless, successful differentiation suggests feasibility in real tissue milieu and reaffirms the findings of the tissue phantom study. Further methodology improvements, for example, via angularly resolved measurements,<sup>40</sup> are envisioned.

## 2 Methods

### 2.1 Experimental Polarimetric System

The configuration and detailed description of the polarimetric system can be found in Ref. 23. Briefly, this setup is designed to generate circularly and linearly polarized light and detect the linear and circular co- and crossed-polarized components in the exact (180 deg) backscattering direction. This was done using a linear polarizer (P1) and quarter-wave retarder (R1) in the illumination axis, and linear analyzer (P2) followed by a quarter-wave retarder (R2) in the detection axis. Samples included microsphere suspensions and teeth, as described below. The light source for the suspensions was a continuous-wave laser diode operating at  $\lambda = 635\text{nm}$ . The light source for the teeth was a continuous-wave helium–neon laser operating at  $\lambda = 543.5\text{ nm}$ . The beam diameter of the light sources was  $\sim 3\text{ mm}$  (full width at half-maximum), with a  $\sim$ Gaussian intensity profile. The detection device was an intensified charge-coupled device (ICCD) camera (PI-MAX<sup>®</sup> 3, Princeton Instruments), which output  $1024 \times 1024$  pixel images, though only the central  $400 \times 400$  pixel region was used for the results reported below. The microsphere suspensions were contained in a plastic cuvette of length 2.2 cm and imaged via a  $2.2 \times 2.2\text{ cm}$  silica optical window. The cuvette was angled slightly off-axis to avoid specular reflection from the air–glass and glass–water interfaces. The teeth were placed in upright positions and the crowns of each tooth were illuminated. Unlike the cuvette, the teeth were angled for maximal detection of specular reflection to enhance optical sensitivity to their surfaces.

### 2.2 Microsphere Suspensions

Monodispersed polystyrene microspheres (Bangs Laboratories, Inc.) of  $d = 1.04\text{ }\mu\text{m}$  diameter were suspended in deionized water to yield a scattering coefficient of  $\mu_s = 25\text{ cm}^{-1}$ , which is approximately the scattering coefficient of the enamel layer of human teeth at  $\lambda \approx 543.5\text{ nm}$ .<sup>41</sup> The spheres had a refractive index of  $n = 1.59$  and the host medium (deionized water) had a refractive index of  $n = 1.33$ .

### 2.3 Tooth Samples and Preparation

Teeth were provided by Dr. Anil Kishen from the University of Toronto School of Dentistry, following standard extraction. Upon visual inspection teeth were considered healthy with an intact enamel surface. Teeth were stored for up to 1 month in ethanol prior to use. Tested teeth included incisors and molars. For artificial induction of demineralization, teeth were oriented

“sideways” and submerged halfway in 37% phosphoric acid (i.e., the biting surface was perpendicular to the acid interface; see the acidification line in Fig. 5). Phosphoric acid at this concentration is commonly used to induce demineralization and emulate natural tooth decay.<sup>42</sup> Seven teeth were studied. Four measurements were taken on each tooth: two on the normal side and two on the acidified side. In total, there were thus 28 data points. Each tooth was submerged for specific times: (tooth 1: 1 min, t2: 5 min, t3: 10 min, t4: 25 min, t5/6/7: 40 min).

#### 2.4 Monte Carlo Simulation Platform

The simulation parameters were configured to match the phantom experiment:  $\sim 10^8$  polarized photon packets ( $\lambda = 635$  nm) were launched into a  $2.2 \times 2.2 \times 2.2$  cm medium of monodispersed  $1.04 \mu\text{m}$  spheres, each with a refractive index of 1.59, suspended in a host refractive index of 1.33. Remaining details and description of the experimentally validated and publicly available Monte Carlo simulation platform<sup>23,43-47</sup> can be found in Ref. 48 and Sec. S1.2 in Ref. 23.

### 3 Theoretical and Experimental Spatial Analysis of Polarimetric Images: Tissue Phantoms

To gain insight into the polarization-dependent backscattering dynamics, we first study single scattering, then connect those concepts to multiple scattering pathways through experimental imaging, corroborated and supplemented by computational modeling-based statistics. To do so, a polystyrene microsphere suspension is employed to greatly simplify the scattering dynamics through its narrow size distribution and discrete bi-phase refractive index profile. This enables convenient simulations of polarized light propagation, for example, as done in our recent studies.<sup>23,47</sup>

The angular distribution of singly scattered polarized light can be calculated by multiplying the Mueller matrix of a sphere with a given Stokes vector:

$$S_{\text{out}} = M_s \times S_{\text{in}} \quad (1)$$

$$\begin{bmatrix} I_{\text{out}} \\ Q_{\text{out}} \\ U_{\text{out}} \\ V_{\text{out}} \end{bmatrix} = \begin{bmatrix} M_{11}(\theta) & M_{12}(\theta) & 0 & 0 \\ M_{12}(\theta) & M_{11}(\theta) & 0 & 0 \\ 0 & 0 & M_{33}(\theta) & M_{34}(\theta) \\ 0 & 0 & -M_{34}(\theta) & M_{33}(\theta) \end{bmatrix} \times \begin{bmatrix} I_{\text{in}} \\ Q_{\text{in}} \\ U_{\text{in}} \\ V_{\text{in}} \end{bmatrix}, \quad (2)$$

$M_s$  represents the Mueller matrix of a single scatterer. The 16 matrix elements can be determined through a Mie scattering calculation; the reader is referred to rigorous textbook summary by Bohren and Huffman<sup>49</sup> for details. The values of the 16 elements also depend on the scattering angle  $\theta$ , the angle between the incident and scattered light vectors (note that the detection plane is kept at a constant azimuthal angle of 0 deg for these calculations).  $S_{\text{out}}$  and  $S_{\text{in}}$  are the scattered and incident Stokes vectors, respectively.

Using Eq. (2), the scattered polarization intensity from a given incident polarization state can be calculated. For example, incident right-circularly polarized  $S_{\text{in}} = [1, 0, 0, 1]^T$  yields the scattered circular polarization intensity of  $V_{\text{out}} = \pm M_{33}$ , where the negative sign indicates orthogonalization (i.e., a helicity-flip such that incident right-circular leaves as left-circular polarization). Interestingly, the scattered 45 deg linear polarization from incident +45 deg linearly polarized light,  $S_{\text{in}} = [1, 0, 1, 0]^T$ , is analogous (equivalent) to the circular case above, expressed as  $U_{\text{out}} = \pm M_{33}$ . Again, the negative sign indicates orthogonalization of the polarization vector (from +45 deg to -45 deg orientation). This equivalency is important conceptually and advantageously technologically in helping measure and interpret the two separate signal channels that detect polarization orthogonalization/preservation.

The scattered circular ( $V_{\text{out}}$ ) and 45 deg linear ( $U_{\text{out}}$ ) polarization intensities from a single polystyrene sphere are theoretically calculated as a function of scattering angle (assuming azimuthal symmetry) and plotted on a polar graph in Fig. 1(a) using Mie parameters  $\lambda = 635$  nm, host refractive index  $n_m = 1.33$  (water), and scatterer refractive index  $n_s = 1.59$  (polystyrene). It is observed that orthogonalization occurs in the backward direction between 135 deg and 225 deg (exact backscattering  $\pm 45$  deg cone). This angular dependency suggests that linearly

orthogonalized photons will exhibit shallower pathways in a polystyrene microsphere suspension (on average), as already shown previously for circularly polarized light.<sup>23</sup> The orthogonalized and preserved (arc-like) pathways are schematized in Fig. 1(b) for incident circularly polarized and 45 deg linearly polarized light to conceptualize the difference in sampling depth. Thus, detection of orthogonalized photons likely enhances sensitivity to reduced sampling depths. Furthermore, due to the equivalency between  $U_{\text{out}}$  and  $V_{\text{out}}$ , they can be used in combination to exploit this sampling depth selectivity effect.

Thus, to maximize superficial-region sensitivity via orthogonalized circular-polarization photons in the backward hemisphere, (1) a cross-circular setup can be employed (which detects helicity-flipped light) and (2) light that is closer to the region of illumination must be selected, as previously shown in fig. 6 in Ref. 23. Indeed, this approach led to an  $\sim 20\%$  reduction in average pathlength.<sup>23</sup> The latter is important since helicity-flipped photons that exist in the radially distant regions arise through randomization/depolarization, which can be deeply penetrating. Circular polarization imaging and associated sampling depth effects were previously explored in detail in Ref. 23; here, we thus focus on linear polarization dynamics and associated image analysis.

Co- and cross-images of backscattered linearly polarized light from the polystyrene microsphere suspension were obtained experimentally [Figs. 2(a) and 2(b)] and through Monte Carlo computational modeling [Figs. 2(c) and 2(d)]. The microsphere suspension was illuminated at the origin by  $-45^\circ$  deg linearly polarized light [incident beam size indicated in Fig. 2(a)]. We will focus our analysis on the simulation images since they are less noisy (easier to analyze) and agree well with the experimental results. Both the co- and cross-linear images exhibit “four-lobed” patterns.<sup>34,36</sup> The co-linear image exhibits lobes along the axes that are parallel and perpendicular to the incident polarization vector (i.e., an “x”-like pattern). The lobes of the cross-linear image form along the regions that are at 45 deg angles with respect to the incident polarization vector (i.e., a “+”-like pattern). Interestingly, the co-linear intensity distributions along the perpendicular axis appear higher than along the parallel axis, resulting in a somewhat asymmetrical oblong image. This may arise from preferential linear polarization preservation

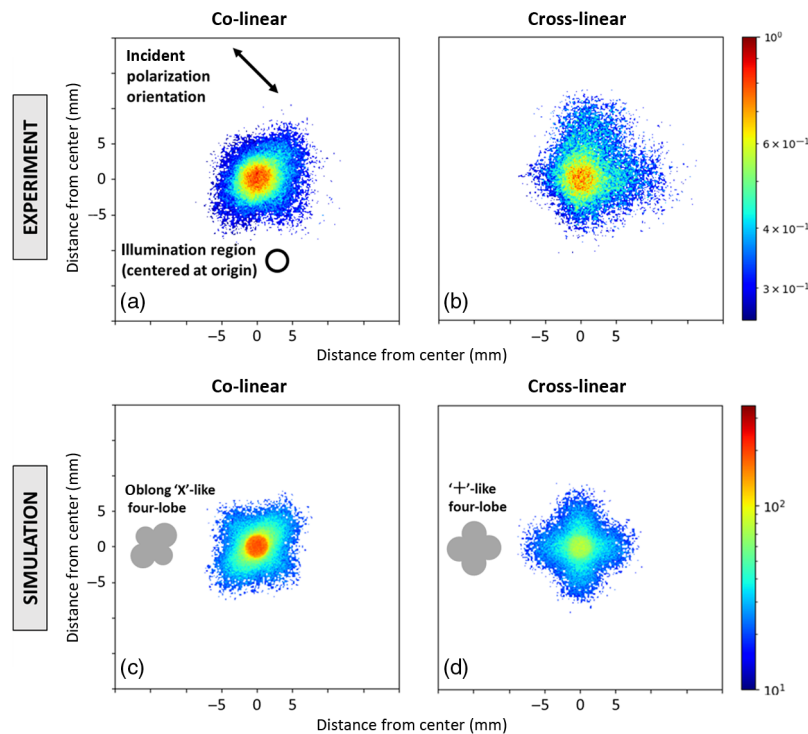


**Fig. 2** (a), (b) Experimental and (c), (d) simulated co-linear and cross-linear images of backscattered linearly polarized light from a  $1.04 \mu\text{m}$  polystyrene microsphere suspension of  $\mu_s = 25 \text{ cm}^{-1}$  turbidity. Co-linear images take on an oblong “x”-like four-lobed pattern, whereas cross-linear images take on a “+”-like four-lobed pattern. These patterns are formed through geometrical effects due to multiple scattering (see text for details).

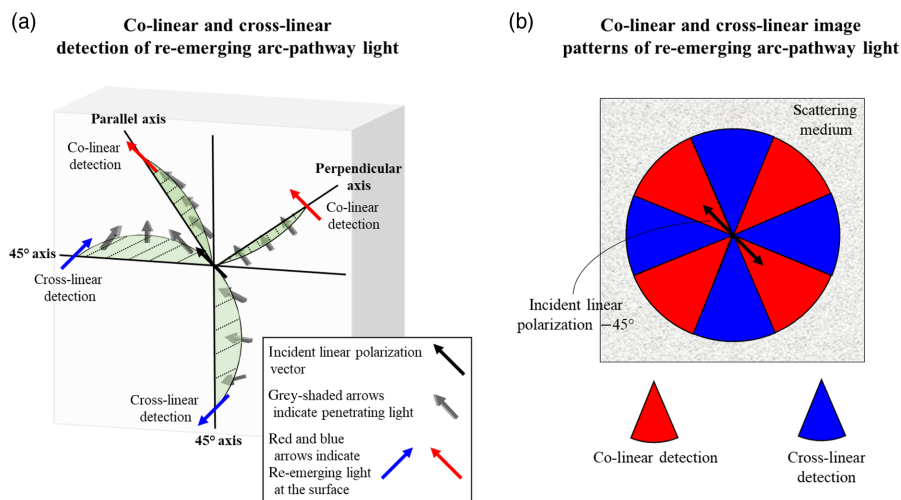


**Fig. 3** Geometrical effects on the linear polarization vector through penetrating arc-like pathways. (a) When linearly polarized light takes an arc-like pathway into the medium along the 45 deg axes, it re-emerges with a crossed orientation with respect to the incident polarization vector (colored blue). Conversely, when the light takes an arc-like pathway into the medium along the parallel or perpendicular axes, the polarization vector re-emerges with its orientation parallel to the incident polarization (colored red). See text for details. (b) Due to the geometric effects of arc-pathways, four-lobed patterns emerge from co- and cross-linear images whereby lobes form along perpendicular and parallel axes (red sectors) or at 45 deg (blue sectors) relative to the incident linear polarization vector, respectively.

through  $\sim$ lateral scattering in the plane perpendicular to the incident linear polarization vector; further investigation is needed to better understand this phenomenon.

The “+”-like pattern of the cross-linear image forms due to a multiple-scattering geometrical reorientation effect of penetrating arc-like pathways on the linear polarization orientation, as visualized in Fig. 3(a) (blue arrows) and Fig. 3(b) (blue sectors). Specifically, when the light takes on a forward-scattering arc-like pathway into the medium, the incident polarization vector can re-emerge with an orientation that is now perpendicular to the incident vector along the axes that are at 45 deg with respect to the incident linear polarization vector.<sup>34</sup> In contrast, the “x”-like patterns form in co-linear images of Fig. 2(c) [and less clearly in Fig. 2(a)] since arc-like pathway light along the axes parallel and perpendicular to the incident polarization vector cannot become crossed due to the symmetry between the pathway direction and that vector. This is visualized by the red arrows in Fig. 3(a) and red sectors in Fig. 3(b).

Another feature of the co-linear images is the detection of the reflection-like orthogonalized light [see Fig. 1(b)] whose polarization orientation remains parallel to the incident linear polarization vector. [This is somewhat counterintuitive since orthogonalization implies that the scattered polarization vector becomes perpendicular to its incident state; however, this is due to the change of reference frame (propagation direction) whereby +45 deg polarization becomes  $-45$  deg in the opposite direction of propagation, despite the physical polarization-axis orientation with respect to the optical table remaining unchanged.] Detection of the orthogonalized light gives rise to a very strong intensity near the illumination region of the co-linear image relative to the cross-linear image as shown in Fig. 2. It is mostly confined to the illumination region since in these interactions the medium essentially acts as a partial mirror at the incidence illumination spot.

Clearly, co- and cross-linear images, and the various spatial patterns within them, are dependent on sub-surface photon propagation pathway dynamics. The sampling depth effects of these linear polarization images can be further investigated through analysis of computational modeling statistics, which appear to be reliable as supported by the reasonable agreement between the simulation and experimental images.

Figure 4 shows the average number of scattering events  $N$  per detected co-linear [Fig. 4(a)] and [Fig. 4(b)] cross-linear photon packet at their corresponding spatial pixel locations. These are

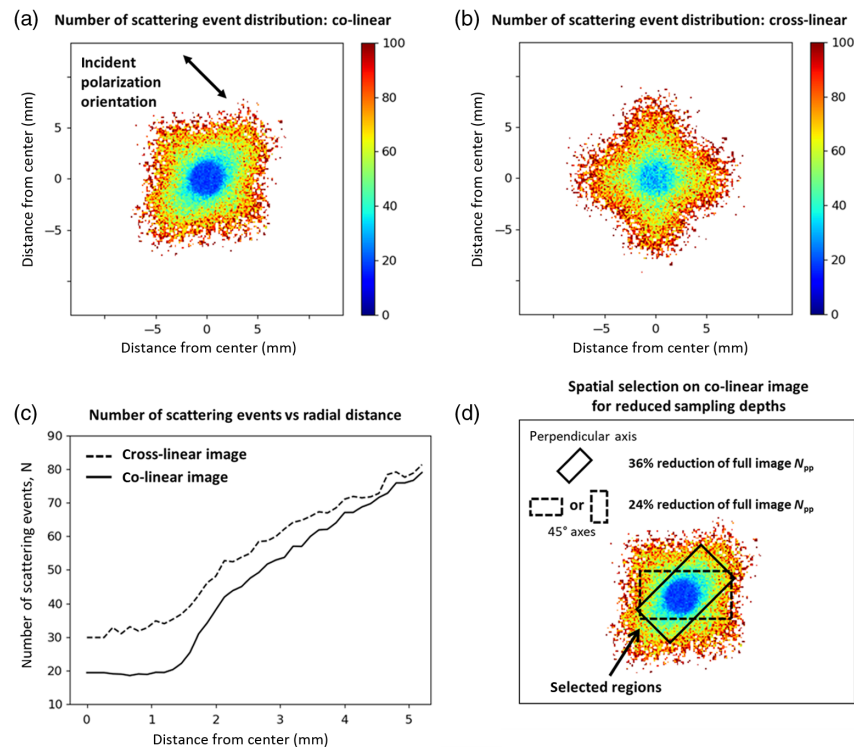


**Fig. 4** Monte Carlo analysis of the number of scattering events yields insight into spatially sensitive sampling depths. (a), (b) Distributions of the number of scattering events per pixel corresponding to the co-linear and cross-linear images in Figs. 2(c) and 2(d). (c) The radial profiles of the co-linear and cross-linear  $N$  distributions showing that the former offers the shallowest sampling (lowest  $N$ ) closer to the illumination region. (d) Sampling depth can be further reduced by selecting pixels within specific regions of the co-linear image (in a). Selecting pixels within the solid-lined rectangle, oriented perpendicularly to the incident polarization vector, reduces the  $N_{pp}$  by 36% relative to that of the full image (see text for details on calculation of  $N_{pp}$ ), as compared to the more modest reduction in  $N_{pp}$  of 24% when selecting pixels within a rectangle oriented along the 45 deg axes (dashed outline).

calculated by dividing the total number of scattering events at each pixel by the corresponding number of detected photons at each pixel [found in the intensity images of Figs. 2(c) and 2(d)]. It is evident that co-linear photons undergo less scattering, particularly in and close to the region of illumination. This is quantitatively shown by the radial profiles of the co- and cross-linear  $N$ -distributions in Fig. 4(c), whereby the largest difference in  $N$  is found at short radial distances; then both curves gradually converge with increasing radial distance until the profiles become  $\sim$ equal, indicating total depolarization. This reaffirms that co-linear polarization detection offers shallower sampling depths (as less scattering implies lower penetration depth).<sup>3</sup>

The oblong shape of the distribution in the co-linear image gives rise to a similarly shaped  $N$ -distribution, with regions along the “long” axis evidently encompassing most of the less-scattered light (low  $N$  values). For example, the light selected within a solid rectangle along that axis, such as the one drawn over the image in Fig. 4(d), appears to have undergone less scattering than if light was selected within a rectangle along any other axis. To test this hypothesis, we calculate the number of scattering events per photon per pixel ( $N_{pp}$ ) within that rectangle when it is oriented along the perpendicular axis (solid outline) and along the vertical or horizontal axis (i.e., the 45 deg axis; dashed outline). These  $N_{pp}$  values are calculated by summing the  $N_{\text{per photon}}$  values at each pixel within the specified region, then dividing by the total number of pixels. As shown in Fig. 4(d), indeed the shallowest sampling depth is achieved through selection of light within the perpendicular axis rectangle, resulting in a 36% reduction of  $N_{pp}$  relative to the  $N_{pp}$  of the full co-linear image, as compared to the 24% reduction of  $N_{pp}$  when selecting light within the rectangle along the 45 deg axes.

It must be noted that one could instead simply select the light in the very sharply defined illumination region [see Figs. 2(c) and 4(a)] to enable the shallowest sampling depths; however, this sharp definition is a result of the flat-field beam used in the simulations (Gaussian beams are currently not supported). Since in practice most laser beams are Gaussian, experimental selection of the illumination region is not as trivial (no sharp cutoff) and the spatial selection discussed above is more practical. Finally, it should also be noted that the results presented in this section likely depends on the medium's anisotropy parameter ( $g$ -factor)<sup>50</sup> and possibly other optical properties; these will be explored in a future study.

Overall, it is shown that co-linear and cross-circular (helicity-flipped) detection are independent signal channels that are sensitive to reflection-like orthogonalized light. This type of light generally penetrates less deeply than the arc-like pathway light, which is much more prominent in cross-linear and co-circular detection configurations. In addition, certain regions within the co-linear and cross-circular images can be selected to further reduce the sampling depth, namely pixels closer to the illumination region (both images) and pixels along the perpendicular axis (co-linear image).

#### 4 Polarimetric Spatial Field Selection: Differentiating Normal and Demineralized Teeth

This reduced-sampling-depth polarimetric approach can be applied to biological tissue to evaluate its potential biomedical utility. We thus employ normal and demineralized teeth as representative tissues that are known to have structurally different surface and sub-surface properties.<sup>51</sup> Differentiation between these tooth types is an important clinical problem, as it can prevent cavities and tooth loss.<sup>38</sup>

Polarimetric measurements were made on each tooth to differentiate the normal and acidified sides with a focus on superficial dental layers (enamel), and the differences between the two groups were quantified. Figures 5(a) and 5(b) show unpolarized and co-linear polarized images of a tooth with a normal side and a 40-min acidified side at 8 $\times$  magnification using a brightfield microscope (Zeiss AxioZoom.V16), respectively. 63 $\times$  magnified co-polarized images of the normal and acidified sides are also shown as insets in Fig. 5(b) where a clear difference in surface topology is observed. Notice that the co-linear polarized image accentuates the surface features by minimizing the contributions of deeply penetrating (depolarized) light to improve contrast between the normal and acidified sides—a visual example of the heightened sensitivity to top dental layers gained by co-linear detection. However, shorter acidification times reduce such visual contrast; for example, the 5-min acidified side of the tooth in Fig. 5(c) is difficult to discern, even at 63 $\times$  magnification (the most prominent difference is likely its reduced glossiness). This highlights the challenge of early tooth decay detection and underscores the need for quantitative analysis.

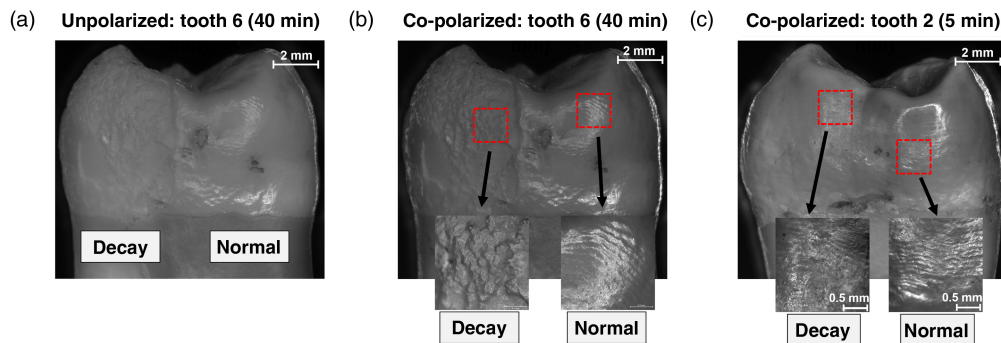


**Fig. 5** (a) Unpolarized and (b) co-linear polarized microscopic images of a tooth with a normal side and a 40-min acidified side (see labels) using a brightfield microscope (Zeiss AxioZoom.V16) at 8 $\times$  magnification. Note that the co-polarized image accentuates the surface features. 63 $\times$  magnified images of both sides of the tooth, shown as insets, exhibit a clear difference in the surface topology. (c) This difference becomes less apparent/indistinguishable for the tooth with a 5-min acidified side, even in the 63 $\times$  magnified images (insets).



The outermost layer of teeth, the enamel, consists primarily of enamel prisms surrounded by calcium hydroxyapatite.<sup>37,38</sup> Early tooth decay typically involves demineralization of the enamel layer whereby bacteria-produced acids in the saliva dissolve the calcium hydroxyapatite.<sup>37</sup> This leads to commonly observed increased surface roughness,<sup>37,51–54</sup> as well as increased scattering (often quantified by the scattering coefficient) just below the surface.<sup>53,55–58</sup> Since specular reflectance decreases with surface roughness,<sup>59</sup> it is expected that orthogonalized light (i.e., specularly reflected light) intensity will be lower for demineralized teeth. Indeed, reduced specular reflectance has previously been observed for demineralized enamel suggesting its potential use for early tooth decay detection,<sup>54</sup> although this study did not consider polarization properties. Furthermore, greater scattering coefficients typically result in higher depolarization.<sup>47,60,61</sup> Thus, it is expected that the backscattered co-linear and cross-circular intensities from demineralized teeth will be lower relative to normal teeth. We explore this conjecture and its further refinement via judicious spatial selection of specific regions in these backscattered polarization images (as per methodology developed in the phantom study).

Analogous to the phantom study, we may gain some theoretical insight into the orthogonalized light response from teeth from their single-scattering Mie optical properties. The thickness of the human enamel layer is estimated to be  $\sim 1.4$  to  $1.7$  mm.<sup>62–65</sup> As average polarized light sampling depths in turbid biological tissues are typically estimated to be  $\sim 2$  mm,<sup>15,16,66–68</sup> and likely much shallower for orthogonalized light, we will only consider the scattering dynamics in the enamel layer. Enamel prisms are thought to be dominant scatterers, surrounded by an inter-prismatic substance consisting of proteins and water.<sup>69</sup> To first order, we can approximate the prisms as spheres,<sup>70</sup> enabling direct use of Mie theory and Stokes-Mueller calculus to compute the single scattering angular distributions of linear and circular polarization intensity. The Mie input parameters for the calculation were: light wavelength in vacuum  $\lambda = 543.5$  nm, host medium refractive index  $n_m = 1.573$  (interprismatic substance<sup>71</sup>), scatterer refractive index  $n_s = 1.619$  (enamel prisms<sup>71</sup>), and scatterer representative linear dimension  $d = 5.75$   $\mu\text{m}$  (prism diameters typically range from  $4$  to  $7.5$   $\mu\text{m}$ <sup>69</sup>). Similar to the polar plot in Fig. 1, Fig. 6 shows that backward-scatter events result in orthogonalization and forward-scattering results in preservation of polarization; the details of the resulting distribution shape are not important due to the uncertainty in the dental properties and calculation assumptions. But overall, we note that orthogonalized light will likely penetrate less deeply [e.g., as schematized in Fig. 1(b)] and is detectable through cross-circular and co-linear polarimetric arrangements.

Figures 7(a) and 7(c) show co-linear and Figs. 7(b) and 7(d) shows cross-circular images of the normal and the 40-min-acidified sides of a tooth [same as shown in Figs. 5(a) and 5(b)]. The

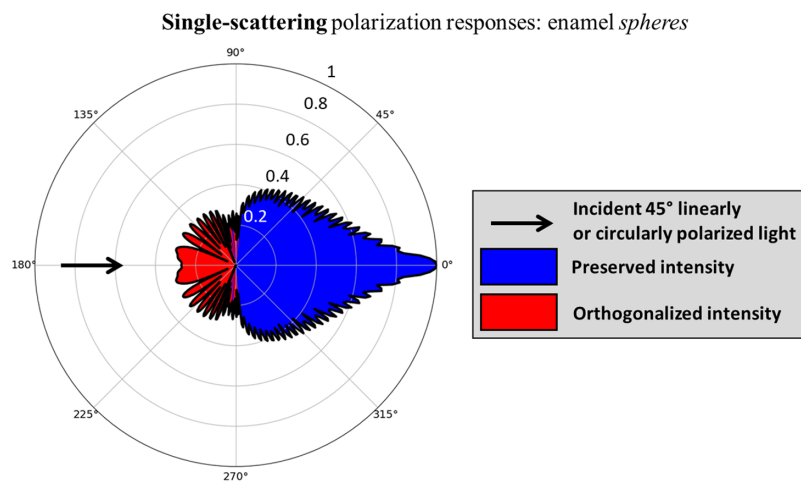


**Fig. 6** Polar plot showing the scattered 45 deg linear and circular polarization intensities from incident 45 deg linearly and circularly polarized light in dental scattering (enamel crystals in hydroxyapatite background). Orthogonalization of the incident polarization state occurs in the backward-hemisphere (90 deg to 270 deg), which likely results in shallower multiple-scattering pathways compared to preserved-polarization light (cf. Fig. 1).

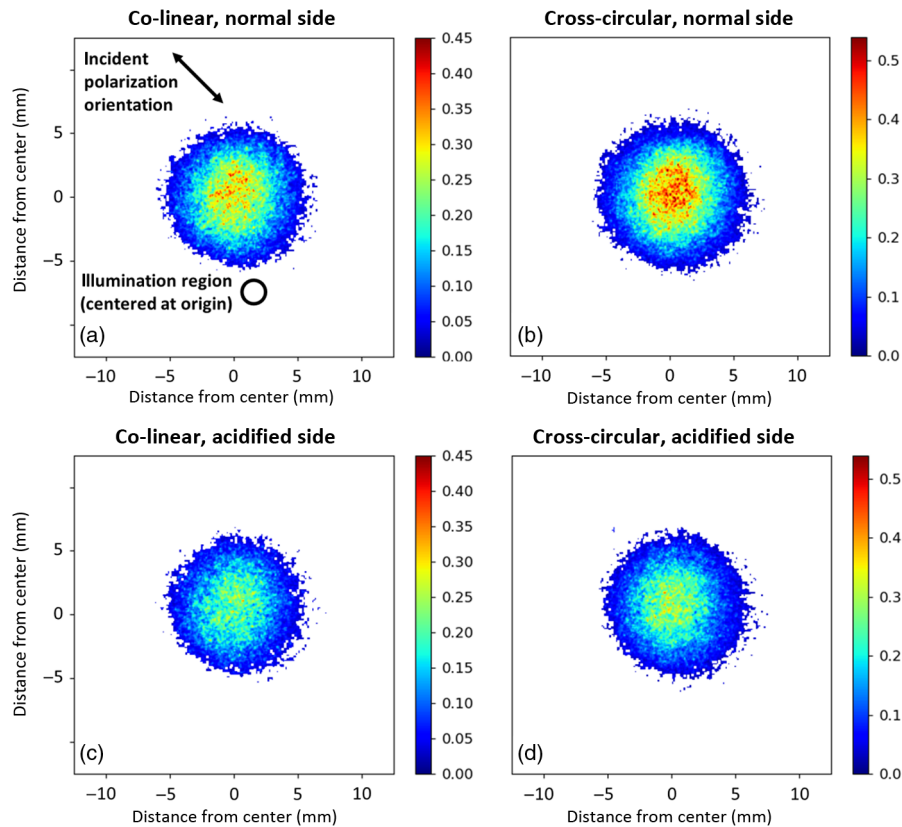


**Fig. 7** (a), (c) Co-linear and (b), (d) cross-circular images of the normal and the 40-min-acidified side of a tooth [same sample as shown in shown in Figs. 5(a) and 5(b)]. There is a clear decrease in the polarization intensities corresponding to the acidified side, attributable to the roughened surface and more depolarizing sub-surface scattering. No spatial patterns are visually apparent in the co-linear images (see text for details).

demineralized side results in noticeably weaker intensities (bottom row compared to top row). However, there is no obvious visibly apparent “x”-like four-lobed pattern in the co-linear images such as those seen in the phantom case of Fig. 2. This may be due to the higher heterogeneity of teeth and broader refractive index and scatterer size distributions compared with the microsphere suspension, yielding a larger depolarized background with more isotropic intensity distributions; however, this is not yet fully understood. There does appear to be somewhat of a higher intensity along the perpendicular axis of many of the co-linear images, for example, in Fig. 7(a), but this is difficult to ascertain qualitatively. Thus, we turn to the quantitative analysis of the spatial-selection methodology developed in the earlier phantom study to quantify polarimetric enamel changes even in this challenging case of visually unobservable patterns.

To test if co-linear and cross-circular intensities are lower in demineralized teeth, the pixel values from the normal and acidified sides of each tooth were summed over the full image and compared using  $t$ -score values. The  $t$ -scores are simple and effective measures of relative difference between the two groups (e.g., intensities from normal and acidified sides),<sup>72</sup> calculated as

$$t\text{-score} = \frac{(\bar{x}_1 - \bar{x}_2)}{\sqrt{S^2 \left( \frac{1}{n_1} + \frac{1}{n_2} \right)}}, \quad (3)$$

where  $\bar{x}_1$  and  $\bar{x}_2$  are the means of the normal and acidified tooth sides, respectively,  $n_1$  and  $n_2$  are the number of data points corresponding to the normal and acidified images, and  $S$  is the standard deviation of all the data points. Indeed, the co-linear and cross-circular image intensities are lower for the demineralized teeth, as shown in the box plots of Figs. 8(a) and 8(c), respectively, yielding  $t$ -scores of 2.34 (co-linear) and 2.71 (cross-circular) with statistically significant

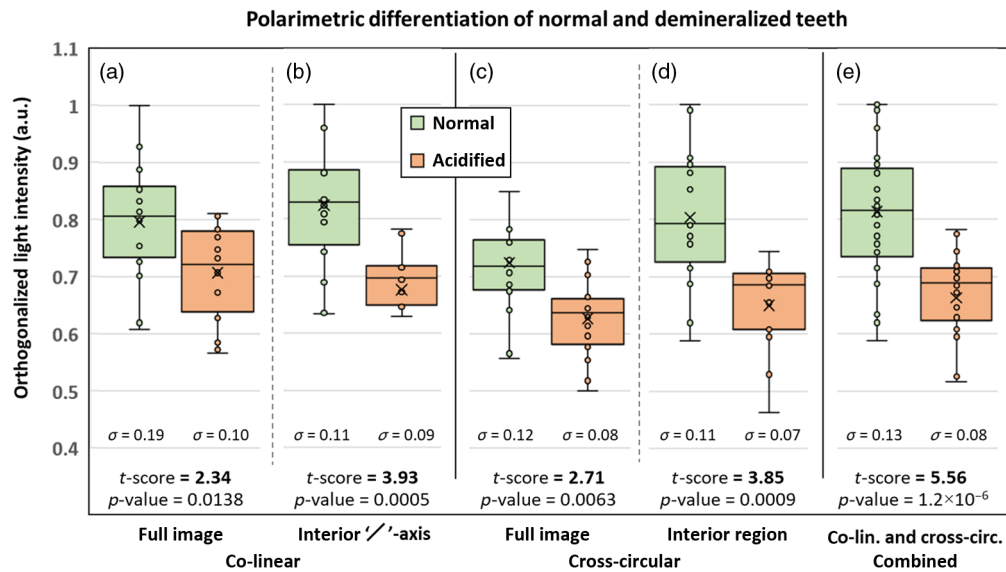


**Fig. 8** Box-and-whisker plots of the intensity metrics corresponding to the normal and acidified sides of the teeth. The individual data points are also shown, as well as the mean values (indicated by the “x” symbols) and standard deviations (denoted by the “ $\sigma$ ” symbols). Five metrics were used to generate five pairs of box-and-whisker plots: summed pixel intensities from (a) the co-linear full image region, (b) co-linear interior perpendicular axis region (denoted by the “//” symbol), (c) cross-circular full image region, and (d) cross-circular interior region. The “interior region” metrics yield the highest separations. (e) The box plot when the data points from both (b) and (d) are included, yielding the highest  $t$ -score via the doubling of the sample size.

separation ( $p$ -values  $< 0.05$ ). The lower intensities are attributed mainly to the roughened surfaces and somewhat to the more depolarizing sub-surfaces.

The spatial selection methods developed in the phantom investigation can be applied to improve this differentiation. Specifically, for circularly polarized light, the pixels within the illumination region are selected for summation, and for linearly polarized light, the pixels along the perpendicular axis within the illumination region are selected for summation. The illumination region encompasses the central pixels within a 3 mm diameter (i.e., the incident beam diameter). The width of the perpendicular axis rectangle is taken as 1/2 of the illumination region diameter (1.5 mm). These dimensions were chosen to best capture light along the perpendicular axis direction while avoiding “crosstalk” from the higher-order scattering along the 45 deg axes’ directions; again, the “optimal” dimensions of this region should be further investigated. As shown in Fig. 8, the intensities of the co-linear perpendicular axis within the interior region [Fig. 8(b)] and the cross-circular interior regions [Fig. 8(d)] yield considerably greater differentiation between normal and demineralized teeth, with  $t$ -scores of 3.93 and 3.85, respectively. Indeed, it appears that the polarimetric spatial field selection approach enhances sensitivity to the superficial regions of the teeth where they are structurally most different. Finally, combining both the cross-linear and co-linear measurements of Figs. 8(b) and 8(d) yields more robust statistical differentiation [Fig. 8(e)] in part due to effectively doubling the sample size (more measurements improve the signal-to-noise ratio). More advanced ways of combining the linear and circular data (e.g., product, ratio, weighted average, etc.) could further improve differentiation and should be investigated.

Another potential method of results analysis is to pair the data points as  $(x, y) = (\text{co-linear intensity, cross-circular intensity})$  from each measured tooth spot to form a “polarimetric map” plot as shown in Fig. 9. The normal-tooth points are mostly separated from the acidified-tooth points. Such a map may be useful in classifying teeth as healthy or decayed upon co-linear and cross-circular measurement. Additional parameters can be incorporated to improve classification accuracy, such as speckle-based metrics, which have shown promise in tooth decay detection<sup>73–75</sup> and can be measured in a polarimetric setup.<sup>76,77</sup> Finally, it appears that the points form a somewhat straight line and their positions may be dependent on surface roughness (e.g., smoother

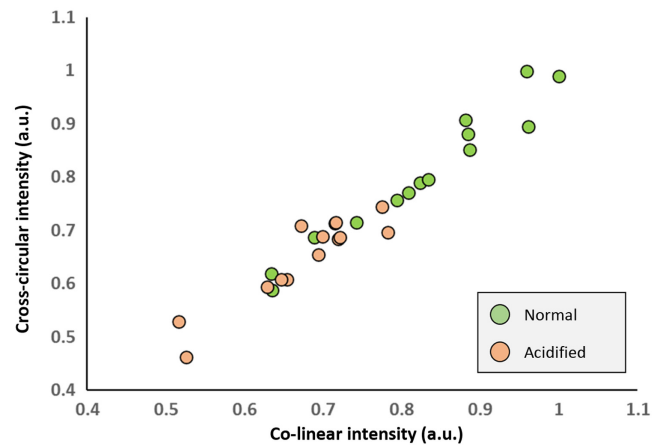


**Fig. 9** Polarimetric mapping of cross-circular and co-linear intensity value pairs shows separation of most normal and acidified data points. This may be useful for classification of these tooth types or potential grading of decay based on datapoint positions (e.g., lower  $x, y$  values indicate severe decay).

surfaces yield higher  $x, y$  values), possibly enabling a calibration line to grade severity of tooth decay.

## 5 Conclusion

Here, it is demonstrated that optical sensitivity to the superficial regions of tissue phantoms and normal/demineralized teeth can be enhanced through a combination of co-linear and cross-circular polarization detection along with judicious spatial selection of specific regions in the backscattered images. In the circular case, the field closer to the illumination region can be selected to reduce the sampling depth. In the linear case, the axis that is perpendicular to the incident linear polarization vector within an area closer to the illumination region can be selected. These results are supported by (1) experimental and computational modeling evidence using polystyrene microsphere suspensions, and (2) experimental polarimetric measurements on normal and demineralized teeth, which are known to differ in their surface/sub-surface structures.

In the future, larger tooth sample sizes should be used to further evaluate the approach for this important clinical problem. This dual-channel polarimetric spatial field selection approach can be combined with other depth-sensitive techniques, such as angular-resolved detection,<sup>40</sup> elliptical polarization measurements,<sup>13–16</sup> and multispectral approaches,<sup>21</sup> for increased control over sampling depths. This may also prove useful for detecting cell nuclear pleomorphism—a hallmark of cancer<sup>78</sup>—during malignant progression in epithelial tissues, where the vast majority of cancers develop (80% to 90%).<sup>79,80</sup> These tissues are mostly cellular and line body surfaces and organs;<sup>81</sup> it is important to maximize signals from these relatively thin superficial linings while minimizing light penetration beyond the epithelial layer—similar to the tooth decay detection problem. Indeed, a powerful polarimetric technique may be formed, which combines this added cellular probing capability to the well-demonstrated collagen sensing via polarization retardance imaging.<sup>82,83</sup>

---

## Disclosures

The authors declare no conflicts of interest.

## Code, Data, and Materials Availability

The datasets used for this study are not publicly available at this time but may be obtained upon reasonable request.

## Acknowledgments

Dr. Daniel Côté (Full Professor, Université Laval) is gratefully acknowledged as the principal developer of the polarization-sensitive Monte Carlo platform. Dr. Anil Kishen (Full Professor, University of Toronto, Faculty of Dentistry) is acknowledged for providing the tooth samples and dental expertise. The authors also acknowledge co-op students Wania Khan (University of British Columbia) and Hunain Jamal (University of Toronto) for their help in the tooth sample preparation process. Finally, we acknowledge Kseniia Tumanova (University of Toronto) for her artistic inputs on the figures.

## References

1. Y. Liu et al., "Investigation of depth selectivity of polarization gating for tissue characterization," *Opt. Express* **13**(2), 601 (2005).
2. R. R. Anderson, "Polarized light examination and photography of the skin," *Arch. Dermatol.* **127**(7), 1000–1005 (1991).
3. S. L. Jacques, J. R. Roman, and K. Lee, "Imaging superficial tissues with polarized light," *Lasers Surg. Med.* **26**(2), 119 (2000).
4. S. L. Jacques, J. C. Ramella-Roman, and K. Lee, "Imaging skin pathology with polarized light," *J. Biomed. Opt.* **7**(3), 329 (2002).
5. V. Backman et al., "Polarized light scattering spectroscopy for quantitative measurement of epithelial cellular structures *in situ*," *IEEE J. Sel. Top. Quantum Electron.* **5**(4), 1019–1026 (1999).
6. V. Backman et al., "Detection of preinvasive cancer cells," *Nature* **406**(6791), 35–36 (2000).
7. R. S. Gurjar et al., "Imaging human epithelial properties with polarized light-scattering spectroscopy," *Nat. Med.* **7**(11), 1245–1248 (2001).
8. G. Jarry et al., "Coherence and polarization of light propagating through scattering media and biological tissues," *Appl. Opt.* **37**(31), 7357 (1998).
9. J. M. Schmitt and S. H. Xiang, "Cross-polarized backscatter in optical coherence tomography of biological tissue," *Opt. Lett.* **23**(13), 1060 (1998).
10. S. G. Demos et al., "Time resolved degree of polarization for human breast tissue," *Opt. Commun.* **124**(5–6), 439–442 (1996).
11. S. G. Demos and R. R. Alfano, "Optical polarization imaging," *Appl. Opt.* **36**(1), 150 (1997).
12. S. Demos, H. Radousky, and R. Alfano, "Deep subsurface imaging in tissues using spectral and polarization filtering," *Opt. Express* **7**(1), 23 (2000).
13. A. da Silva et al., "Depth selectivity in biological tissues by polarization analysis of backscattered light," *Proc. SPIE* **8172**, 817205 (2011).
14. S. Rehn et al., "Depth probing of diffuse tissues controlled with elliptically polarized light," *J. Biomed. Opt.* **18**(1), 016007 (2013).
15. S. Sridhar and A. Da Silva, "Enhanced contrast and depth resolution in polarization imaging using elliptically polarized light," *J. Biomed. Opt.* **21**(7), 071107 (2016).
16. A. Da Silva, C. Deumié, and I. Vanzetta, "Elliptically polarized light for depth resolved optical imaging," *Biomed. Opt. Express* **3**(11), 2907 (2012).
17. J. M. Schmitt, A. H. Gandjbakhche, and R. F. Bonner, "Use of polarized light to discriminate short-path photons in a multiply scattering medium," *Appl. Opt.* **31**(30), 6535 (1992).
18. A. J. Gomes and V. Backman, "Analytical light reflectance models for overlapping illumination and collection area geometries," *Appl. Opt.* **51**(33), 8013 (2012).
19. S. Ruderman et al., "Analysis of pressure, angle and temporal effects on tissue optical properties from polarization-gated spectroscopic probe measurements," *Biomed. Opt. Express* **1**(2), 489 (2010).
20. Y. Liu, Y. L. Kim, and V. Backman, "Development of a bioengineered tissue model and its application in the investigation of the depth selectivity of polarization gating," *Appl. Opt.* **44**(12), 2288–2299 (2005).
21. A. Pierangelo et al., "Multispectral Mueller polarimetric imaging detecting residual cancer and cancer regression after neoadjuvant treatment for colorectal carcinomas," *J. Biomed. Opt.* **18**(4), 046014 (2013).
22. H. Arimoto, "Multispectral polarization imaging for observing blood oxygen saturation in skin tissue," *Appl. Spectrosc.* **60**(4), 459–464 (2006).
23. M. D. Singh and I. A. Vitkin, "Spatial helicity response metric to quantify particle size and turbidity of heterogeneous media through circular polarization imaging," *Sci. Rep.* **13**(1), 2231 (2023).
24. A. D. Kim and M. Moscoso, "Backscattering of circularly polarized pulses," *Opt. Lett.* **27**(18), 1589 (2002).
25. X. Ni and R. R. Alfano, "Time-resolved backscattering of circularly and linearly polarized light in a turbid medium," *Opt. Lett.* **29**(23), 2773 (2004).
26. K. G. Phillips et al., "Time-resolved ring structure of circularly polarized beams backscattered from forward scattering media," *Opt. Express* **13**(20), 7954 (2005).

27. M. Sakami and A. Dogariu, "Polarized light-pulse transport through scattering media," *J. Opt. Soc. Am. A* **23**(3), 664 (2006).
28. W. T. Cope, M. L. Wolbarsht, and B. S. Yamanashi, "The corneal polarization cross," *J. Opt. Soc. Am.* **68**(8), 1139–1141 (1978).
29. B. F. Hochheimer and H. A. Kues, "Retinal polarization effects," *Appl. Opt.* **21**(21), 3811 (1982).
30. B. K. Pierscionek and R. A. Weale, "Is there a link between corneal structure and the 'corneal cross'?" *Eye* **11**(3), 361–364 (1997).
31. A. I. Carswell and S. R. Pal, "Polarization anisotropy in LiDAR multiple scattering from clouds," *Appl. Opt.* **19**(24), 4123 (1980).
32. S. R. Pal and A. I. Carswell, "Polarization anisotropy in LiDAR multiple scattering from atmospheric clouds," *Appl. Opt.* **24**(21), 3464 (1985).
33. Y. Kuga, L. Tsang, and A. Ishimaru, "Depolarization effects of the enhanced retroreflectance from a dense distribution of spherical particles," *J. Opt. Soc. Am. A* **2**(4), 616 (1985).
34. M. Dogariu and T. Asakura, "Polarization-dependent backscattering patterns from weakly scattering media," *J. Opt.* **24**(6), 271–278 (1993).
35. M. Dogariu, "Photon pathlength distribution from polarized backscattering in random media," *Opt. Eng.* **35**(8), 2234 (1996).
36. A. H. Hielscher, J. R. Mourant, and I. J. Bigio, "Influence of particle size and concentration on the diffuse backscattering of polarized light from tissue phantoms and biological cell suspensions," *Appl. Opt.* **36**(1), 125 (1997).
37. J. Gomez, "Detection and diagnosis of the early caries lesion," *BMC Oral Health* **15**(S1), S3 (2015).
38. N. B. Pitts et al., "Dental caries," *Nat. Rev. Dis. Primers* **3**(1), 17030 (2017).
39. D. Fried, "Lasers and optics for measuring tooth decay," *Opt. Photonics News* **21**(4), 14 (2010).
40. A. Wax et al., "In situ detection of neoplastic transformation and chemopreventive effects in rat esophagus epithelium using angle-resolved low-coherence interferometry," *Cancer Res.* **63**(13), 3556–3559 (2003).
41. D. Spitzer and J. J. Ten Bosch, "The absorption and scattering of light in bovine and human dental enamel," *Calcif. Tissue Res.* **17**(2), 129–137 (1975).
42. S. Paris et al., "Micro-hardness and mineral loss of enamel lesions after infiltration with various resins: influence of infiltrant composition and application frequency *in vitro*," *J. Dent.* **41**(6), 543–548 (2013).
43. D. Côté and I. A. Vitkin, "Pol-MC: a three dimensional polarization sensitive Monte Carlo implementation for light propagation in tissue," <http://www.novajo.ca/ont-canc-inst-biophotonics> (2005).
44. M. F. G. Wood, X. Guo, and I. A. Vitkin, "Polarized light propagation in multiply scattering media exhibiting both linear birefringence and optical activity: Monte Carlo model and experimental methodology," *J. Biomed. Opt.* **12**(1), 014029 (2007).
45. X. Guo, M. F. G. Wood, and I. A. Vitkin, "Stokes polarimetry in multiply scattering chiral media: effects of experimental geometry," *Appl. Opt.* **46**(20), 4491–4500 (2007).
46. N. Ghosh, M. F. G. Wood, and I. A. Vitkin, "Mueller matrix decomposition for extraction of individual polarization parameters from complex turbid media exhibiting multiple scattering, optical activity, and linear birefringence," *J. Biomed. Opt.* **13**(4), 044036 (2008).
47. M. D. Singh and I. A. Vitkin, "Discriminating turbid media by scatterer size and scattering coefficient using backscattered linearly and circularly polarized light," *Biomed. Opt. Express* **12**(11), 6831 (2021).
48. D. Cote and I. A. Vitkin, "Robust concentration determination of optically active molecules in turbid media with validated three-dimensional polarization sensitive Monte Carlo calculations," *Opt. Express* **13**(1), 148–163 (2005).
49. C. F. Bohren and D. R. Huffman, "Absorption and scattering by a sphere," in *Absorption and Scattering of Light by Small Particles*, Vol. 7, pp. 82–129, Wiley-VCH Verlag GmbH (2007).
50. A. Doronin, C. Macdonald, and I. Meglinski, "Propagation of coherent polarized light in turbid highly scattering medium," *J. Biomed. Opt.* **19**(2), 025005 (2014).
51. J. Field, P. Waterhouse, and M. German, "Quantifying and qualifying surface changes on dental hard tissues *in vitro*," *J. Dent.* **38**(3), 182–190 (2010).
52. X. Z. Zhang et al., "Optical profilometric study of changes in surface roughness of enamel during *in vitro* demineralization," *Caries Res.* **34**(2), 164–174 (2000).
53. M. T. Tsai et al., "Early detection of enamel demineralization by optical coherence tomography," *Sci. Rep.* **9**(1), 17154 (2019).
54. E. Rakhmatullina et al., "Application of the specular and diffuse reflection analysis for *in vitro* diagnostics of dental erosion: correlation with enamel softening, roughness, and calcium release," *J. Biomed. Opt.* **16**(10), 107002 (2011).
55. M. G. Sowa et al., "A comparison of methods using optical coherence tomography to detect demineralized regions in teeth," *J. Biophotonics* **4**(11–12), 814–823 (2011).
56. T. Louie et al., "Clinical assessment of early tooth demineralization using polarization sensitive optical coherence tomography," *Lasers Surg. Med.* **42**(10), 898–905 (2010).

57. D. Fried et al., "Imaging caries lesions and lesion progression with polarization sensitive optical coherence tomography," *J. Biomed. Opt.* **7**(4), 618 (2002).
58. D. Spitzer and J. J. Ten Bosch, "Luminescence quantum yields of sound and carious dental enamel," *Calcif. Tissue Res.* **24**(1), 249–251 (1977).
59. H. E. Bennett and J. O. Porteus, "Relation between surface roughness and specular reflectance at normal incidence," *J. Opt. Soc. Am.* **51**(2), 123 (1961).
60. N. Ghosh et al., "Depolarization of light in tissue phantoms: effect of collection geometry," *Opt. Commun.* **222**(1–6), 93–100 (2003).
61. V. Sankaran et al., "Comparison of polarized-light propagation in biological tissue and phantoms," *Opt. Lett.* **24**(15), 1044 (1999).
62. S. A. Fernandes et al., "Crown dimensions and proximal enamel thickness of mandibular second bicuspid," *Braz. Oral Res.* **25**(4), 324–330 (2011).
63. E. Beniash et al., "The hidden structure of human enamel," *Nat. Commun.* **10**(1), 4383 (2019).
64. D. M. Daubert et al., "Human enamel thickness and ENAM polymorphism," *Int. J. Oral Sci.* **8**(2), 93–97 (2016).
65. N. K. Ravichandran et al., "Micron-scale human enamel layer characterization after orthodontic bracket debonding by intensity-based layer segmentation in optical coherence tomography images," *Sci. Rep.* **11**(1), 10831 (2021).
66. X. Wang and L. V. Wang, "Propagation of polarized light in birefringent turbid media: a Monte Carlo study," *J. Biomed. Opt.* **7**(3), 279 (2002).
67. N. Nishizawa and T. Kuchimaru, "Depth estimation of tumor invasion in early gastric cancer using scattering of circularly polarized light: Monte Carlo simulation study," *J. Biophotonics* **15**(10), e202200062 (2022).
68. X. Guo, M. F. G. Wood, and A. Vitkin, "Monte Carlo study of pathlength distribution of polarized light in turbid media," *Opt. Express* **15**(3), 1348 (2007).
69. A. A. Kunin, A. Y. Evdokimova, and N. S. Moiseeva, "Age-related differences of tooth enamel morphochemistry in health and dental caries," *EPMA J.* **6**(1), 3 (2015).
70. S. P. Neshyba, T. C. Grenfell, and S. G. Warren, "Representation of a nonspherical ice particle by a collection of independent spheres for scattering and absorption of radiation: 2. Hexagonal columns and plates," *J. Geophys. Res.: Atmos.* **108**(15), 1–18 (2003).
71. J. R. Zijp, J. J. Ten Bosch, and R. A. J. Groenhuis, "HeNe-laser light scattering by human dental enamel," *J. Dent. Res.* **74**(12), 1891–1898 (1995).
72. M. Mahbobi and T. K. Tiemann, "Chapter 2. The normal and t-distributions," in *Introductory Business Statistics with Interactive Spreadsheets – 1st Canadian Edition*, BCcampus (2015).
73. A. M. Deana et al., "Detection of early carious lesions using contrast enhancement with coherent light scattering (speckle imaging)," *Laser Phys.* **23**(7), 075607 (2013).
74. N. H. Koshiji et al., "Laser speckle imaging: a novel method for detecting dental erosion," *PLoS One* **10**(2), e0118429 (2015).
75. C. A. Nader et al., "Early diagnosis of teeth erosion using polarized laser speckle imaging," *J. Biomed. Opt.* **21**(7), 071103 (2015).
76. L. Tchvialeva et al., "Polarization speckle imaging as a potential technique for *in vivo* skin cancer detection," *J. Biomed. Opt.* **18**(6), 061211 (2012).
77. D. C. Louie et al., "Constructing a portable optical polarimetry probe for *in-vivo* skin cancer detection," *J. Biomed. Opt.* **26**(03), 035001 (2021).
78. WHO Classification of Tumor Editorial Board, *Soft Tissue and Bone Tumours WHO Classification of Tumours*, Vol. **3**, 5th ed., International Agency for Research on Cancer (2020).
79. L. Hinck and I. Näthke, "Changes in cell and tissue organization in cancer of the breast and colon," *Curr. Opin. Cell Biol.* **26**(1), 87–95 (2014).
80. National Cancer Institute, "National Cancer Institute - cancer classification," <https://training.seer.cancer.gov/disease/categories/classification.html> (2023).
81. National Cancer Institute, "National Cancer Institute - epithelial tissue," [https://training.seer.cancer.gov/anatomy/cells\\_tissues\\_membranes/tissues/epithelial.html](https://training.seer.cancer.gov/anatomy/cells_tissues_membranes/tissues/epithelial.html) (2023).
82. J. Qi et al., "Surgical polarimetric endoscopy for the detection of laryngeal cancer," *Nat. Biomed. Eng.* 1–15 (2023).
83. M. D. Singh, N. Ghosh, and I. A. Vitkin, "Mueller matrix polarimetry in biomedicine: enabling technology, biomedical applications, and future prospects," in *Polarized Light in Biomedical Imaging and Sensing*, J. C. Ramella-Roman and T. Novikova, Eds., pp. 61–103, Springer International Publishing (2023).

**Michael D. Singh** is a PhD candidate at the University of Toronto in the medical biophysics graduate program in the Temerty Faculty of Medicine and performs his research at the Princess Margaret Cancer Centre. His current research is focused on polarized light scattering dynamics in turbid media to discover novel ways to optically probe and characterize biological tissues.

Previously, he studied molecular imaging and material ablation using femtosecond and nanosecond laser pulses at the University of Waterloo where he received his MSc degree.

**Lothar Lilge** received his PhD from Westfaehliche Wilhelms University in Muenster, Germany, and postdoctoral training at the Wellman Laboratory of Photomedicine in Boston, Massachusetts, USA, and the McMaster University in Hamilton, Ontario, Canada. His current research projects are focusing on photodynamic therapy, in particular developing new treatment planning approaches, and on optical spectroscopic diagnostics to identify women with an elevated risk of developing breast cancer.

**Alex Vitkin** is a professor of medical biophysics and radiation oncology at the University of Toronto, a senior scientist at the Princess Margaret Cancer Research Institute, and a clinical medical physicist at Princess Margaret Cancer Centre (Toronto, Ontario, Canada). He has published over 180 papers and book chapters on diagnostic and therapeutic uses of light in biomedicine, focusing on tissue polarimetry and functional optical coherence tomography. He is a board-certified medical physicist and a fellow of Optica, AIMBE, and SPIE.